The Astrophysical Journal, 576:832–848, 2002 September 10

HYDRODYNAMIC INTERACTION OF STRONG SHOCKS WITH INHOMOGENEOUS MEDIA. I. ADIABATIC CASE

A. Y. Poludnenko, A. Frank, and E. G. Blackman
Department of Physics and Astronomy, University of Rochester, Rochester, NY 14627-0171;
wma@pas.rochester.edu, afrank@pas.rochester.edu, blackman@pas.rochester.edu
Received 2001 September 12; accepted 2002 May 20

ABSTRACT

Many astrophysical flows occur in inhomogeneous (clumpy) media. We present results of a numerical study of steady, planar shocks interacting with a system of embedded cylindrical clouds. Our study uses a two-dimensional geometry. Our numerical code uses an adaptive mesh refinement, allowing us to achieve sufficiently high resolution both at the largest and the smallest scales. We neglect any radiative losses, heat conduction, and gravitational forces. Detailed analysis of the simulations shows that interaction of embedded inhomogeneities with the shock/postshock wind depends primarily on the thickness of the cloud layer and arrangement of the clouds in the layer. The total cloud mass and the total number of individual clouds is not a significant factor. We define two classes of cloud distributions: thin and thick layers. We define the critical cloud separation along the direction of the flow and perpendicular to it, distinguishing between the interacting and noninteracting regimes of cloud evolution. Finally, we discuss mass loading and mixing in such systems.

Subject headings: hydrodynamics — ISM: clouds — planetary nebulae: general — shock waves — stars: mass loss

1. INTRODUCTION

Mass outflows play a critical role in many astrophysical systems, ranging from stars to the most distant active galaxies. Virtually all studies of mass outflows to date have focused on flows in homogeneous media. However, the typical astrophysical medium is inhomogeneous, with the "clumps" or "clouds" arising on a variety of scales. These inhomogeneities may arise because of initial fluctuations of the ambient mass distribution, the action of instabilities, variations in the flow source, etc. Whatever the origin of the clumps, their effect can be dramatic. The presence of inhomogeneities can introduce not only quantitative but also qualitative changes to the overall dynamics of the flow.

A number of studies have attempted to understand the role of embedded inhomogeneities via (primarily) analytical methods (Hartquist et al. 1986; Hartquist & Dyson 1988; Dyson & Hartquist 1992, 1994; Redman, Williams, & Dyson 1998). In these pioneering works it was suggested that interactions of the global flow with inhomogeneities may cause significant changes in the physical, dynamical, and even chemical state of the system. Two major consequences of the presence of clumps are mass loading (i.e., seeding of material, ablated from the surface of inhomogeneities, into the global flow) and transition of the global flow into a transonic regime irrespective of the initial conditions. The papers cited above considered the potential effects of mass loading on the global properties of a number of objects in which inhomogeneities can be resolved. Such objects include planetary nebulae, e.g., NGC 2392 (O'Dell, Weiner, & Chu 1990; Phillips & Cuesta 1999) and NGC 7293 (Burkert & O'Dell 1998), Wolf-Rayet stars, primarily RCW 58, which is believed to be mass-loading–dominated (Hartquist et al. 1986; Arthur, Henney, & Dyson 1996), and others.

A number of numerical studies of *single-clump* interactions have been performed (Klein, McKee, & Colella 1994, hereafter KMC94; Anderson et al. 1994; Jones, Ryu, & Tregillis 1996; Gregori et al. 1999, 2000; Jun & Jones 1999; Miniati, Jones, & Ryu 1999; Lim & Raga 1999). In these papers, the basic hydrodynamics or MHD of wind-clump and shock-clump physics have been detailed (often with microphysical processes included). A few studies of shock waves overrunning over multiple clumps exist in the literature (e.g., Jun, Jones, & Norman 1996). A detailed study of multiple clumps, however, where an attempt is made to articulate basic physical processes and differentiate various parameter regimes, has not yet been carried out. In this paper (and those that follow) we address the problem of clumpy flows, providing a description of the dynamics of multiple dense clouds interacting with a strong, steady planar shock.

The large parameter space and complexity of the problem require significant computational effort. To provide the necessary resolution of the flow, we have used an adaptive mesh refinement method. This is a relatively new computational technology, and because of this we have chosen to investigate so-called adiabatic flows, in which radiative cooling is not considered. In this regard our approach is similar to that described by Klein et al. (1994) for single clumps, and we utilize their results in understanding our multiclump simulations. We note that preliminary results, appropriate to active galactic nuclei (AGNs), were presented in Poludnenko, Frank, & Blackman (2002).

The plan of the paper is as follows. In § 2 we describe the numerical experiments, the code used, and the formulation of the problem. In § 3.1 we consider the general properties of the shock-cloud interaction in the context of the multicloud systems; primarily we focus on the four major phases of the interaction process. In § 3.2 we discuss the role of cloud distribution in determining the dynamics of the system evolution. In § 3.3 we define several key parameters that allow us to distinguish between various regimes of shock-cloud interaction. Finally, in § 3.4 we address the issue of mass loading in such systems.

2. NUMERICAL EXPERIMENTS

2.1. *Description of the Code Used*

The code we used for this project is the AMRCLAW package, which implements an adaptive mesh refinement algorithm for the equations of gasdynamics (Berger & LeVeque 1998; Berger & Jameson 1985; Berger & Colella 1989; Berger & Oliger 1984). In the AMRCLAW approach, the computational domain is associated with a logically rectangular grid that represents the lowest level of refinement (level 1) and that embeds the nested sequence of logically rectangular meshes with finer resolution (levels 2, 3, ...). The temporal and spatial steps of all grids at a level L are refined with respect to the level $L-1$ grids by the same factor, typically 4 in our calculations. The mesh ratios $\Delta t/\Delta x$ and $\Delta t/\Delta y$ are then the same on all grids, ensuring stability with explicit difference schemes.

The solution on each grid is advanced via a second-order–accurate Godunov-type finite-volume method in which second-order accuracy is achieved via flux-limiting and proper consideration of transverse wave propagation. The multidimensional wave-propagation algorithm is based on the traditional dimensional splitting with the Riemann problem solved in each dimension by means of a Roe-approximate Riemann solver (LeVeque 1997). It should be noted that our implementation of the Riemann solver, based on the Roe linearization, does not use any additional procedures to ensure satisfaction of the entropy condition, as usually employed for this type of Riemann solver. Our analysis shows that the numerical diffusion present in the system is sufficient to prevent entropy-violating waves from propagating in the system.

The hydrodynamic equations we solve are appropriate to a single-fluid system, although a passive tracer is introduced in order to track advection and mixing of the cloud material. This was implemented as an additional wave family in the Roe solver.

Our numerical experiments were performed on a coarse grid with the resolution of 50×100 cells and with the maximum number of refinement levels equal to 3 (meaning that the coarse grid associated with the computational domain embeds not more than two nested higher resolution levels). Each higher level has a temporal and spatial step refined by the factor of 4 in comparison with the next lowest level, and we kept this refinement ratio constant for all levels. Such a setup provides the equivalent resolution[1] of 800×1600 cells. In order to facilitate comparison of our numerical experiments with those of KMC94, we describe the resolution not in terms of the equivalent resolution but in terms of the number of cells that fit in the original maximal cloud radius a_0, following the convention of KMC94. Then all of the runs described here in our paper have 32 cells per cloud radius.

KMC94 suggested that a minimum resolution of 120 cells per cloud radius is necessary. We have performed the simulations of the cloud-shock interaction with the resolution of 120, 75, and 55 cells per cloud radius. Although we do not describe the details of those runs in this paper, the principal difference between the cases with maximum and minimum resolution, i.e., 120 and 32 cells per cloud radius, is the rate of instability formation at the boundary layers.[2] This does not seem to have any significant effect on the global properties of the interaction or the averaged characteristics of the individual cloud ablation processes. Therefore, we find the resolution of 30 cells per cloud radius and above to represent accurately the global properties of the interaction process under consideration. Moreover, 30 cells per cloud radius is a reasonable compromise between maximizing the size of the computational domain and capturing as many small-scale features of the interaction process as possible. We emphasize that our problem requires a compromise between the resolution needed for simulating details of individual cloud structures and capturing the global flow pattern.

Finally, another aspect of this problem is the connection between the spatial resolution (which naturally sets the smallest scale resolvable in the simulations) and the diffusion and thermal conduction length scales. As we show in § 3.1.4, viscous diffusion and thermal conduction in a real physical system operate at length scales comparable to the size of a computational cell at the highest refinement level used in our simulations. Therefore, in a real system, features smaller than the ones that can be resolved with our resolution could not survive over the dynamical timescales relevant to the problem. We will address this in greater detail when we discuss the mixing phase of cloud evolution. Of course, numerical diffusion must also be considered but, as discussed above, our compromise resolution appears to satisfy the need to capture both small- and large-scale behavior.

2.2. *Formulation of the Problem*

We set up a two-dimensional computational volume, associated with the initial condition of N different clouds of radius a_i and density ρ_i embedded in the ambient medium of density ρ_a, and an incident shock wave. Since all of the experiments were performed in the Cartesian geometry, the clouds are actually cross sections of the infinitely long cylinders. We will address the importance of the cloud shape in more detail in subsequent work, where we will consider the fully three-dimensional case of the shock interaction with spherical clouds. Denoting the maximum cloud radius present in the system as $a_{\max}$, our computational domain is $25a_{\max} \times 50a_{\max}$. This allows us to track the dynamical evolution of the system over greater temporal and spatial intervals compared to the $6a_{\max} \times 16a_{\max}$ domain considered by KMC94.

All our calculations were performed in a fixed reference frame in which both the clouds and the ambient medium are stationary at time $t = 0$. In this reference frame the horizontal axis is taken to be the x-axis, and the vertical axis the y-axis. Initially, both the clouds and the surrounding intercloud medium are assumed to be in pressure equilibrium and have pressure P_0. Typically, the extent of the region occupied by the cloud distribution at time $t = 0$ is taken to be not more than 30%–35% of the horizontal extent of the computational domain with X_L offset by 5% from the left boundary of the computational domain and X_R offset by 35%–40%. Table 1 below, describing the numerical experiments discussed in this paper, provides the details of the

[1] By equivalent resolution hereafter we mean the resolution of a uniform grid covering all of the computational domain and possessing the temporal and spatial step of the highest refinement level.

[2] For the case of lower resolution, the lower rate of instability formation may be somewhat compensated by the use of the compressive flux limiters.

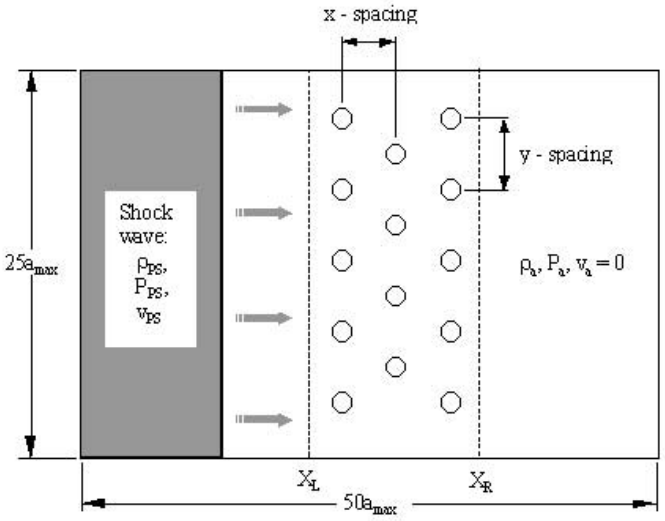

FIG. 1.—Setup of the computational domain. Shown is the setup for the run M14. The "x-spacing" and "y-spacing" are the parameters used in Table 1 for the description of the runs. Note that this is not drawn to scale.

cloud distribution in each simulation. Figure 1 illustrates the setup of the computational domain at $t = 0$.

In the most general case, we assume each cloud to have the same nonuniform density profile. The clouds have constant density up to a smoothing transition region at the cloud edge, which is achieved through a linear or $\tanh(r)$ function. We typically set the extent of the transition region to the outer 20% of a cloud radius a_i and use the $\tanh(r)$-type smoothing function. Therefore, the cloud density profile is of the form

$$\rho_i(r) = \begin{cases} \rho_i = \text{const} , & 0 \le r \le r_i , \\ \dfrac{\rho_a + \rho_i}{2} + \dfrac{\rho_a - \rho_i}{2} \dfrac{\tanh[r - (a_i + r_i)/2]}{\tanh[(a_i - r_i)/2]} & r_i \le r \le a_i , \end{cases} \quad (1)$$

Although there is very little observational data available concerning the internal structure of embedded clouds, this particular choice of the density profile seems to be a sufficiently good approximation to the real physical clouds and inhomogeneities.

In the simple adiabatic interaction of a cloud with a shock wave, there are two dimensionless parameters that completely define the problem: the Mach number of the blast wave, M_S, and the density contrast between the cloud and the intercloud medium,

$$\chi_i \equiv \frac{\rho_i}{\rho_a} . \quad (2)$$

The range of values spanned by the density contrast χ can be quite large and is the most important parameter of the problem. For the astrophysical situations of interest, this range can often cover up to 5 orders of magnitude (from 10 to 10^6), presenting a significant challenge both for the numerical modeling and for the subsequent interpretation and analysis of the results. In order to decrease the extent of this dimension of the parameter space, we chose a "compromise" value of the parameter χ to be 500. Although the runs we discuss in this paper all use this value of the density contrast, we briefly discuss numerical experiments with $10 \lesssim \chi \lesssim 1000$ in the results section, particularly in the context of the problem of mass loading. We will provide a more comprehensive study of scaling with density contrast in the subsequent work.

Another important parameter is the shock-wave Mach number M_S, defined with respect to the ambient medium sound speed $C_a = (\gamma P_0/\rho_a)^{1/2}$. We consider a planar, steady, strong shock wave propagating into the computational domain from the left. Since we operate in the reference frame in which both the clouds and the ambient medium are stationary, the shock-wave Mach number completely defines the shock velocity as well as the conditions of the postshock flow. The conditions in the postshock flow, namely the postshock density $\rho_{\rm PS}$, pressure $P_{\rm PS}$, and velocity $v_{\rm PS}$, are determined using the Rankine-Hugoniot relations in the usual manner (Landau & Lifshitz 1959).[3]

Shock-wave Mach numbers in astrophysical situations can cover a large range of values. However, for strong shocks the problem becomes practically independent of the Mach number.[4] Indeed, the results of KMC94 show that for the difference in M_S of 2 orders of magnitude (10–1000), time evolution of the system does not differ by more than 15%. We will see that our analytical results fully corroborate the presence of Mach scaling in the problem under consideration.

We assume that the structure of the postshock flow does not change in time for the duration of the simulations. An example of such steady postshock flow is the wind from a post-AGB star driving a shock with a constant postshock flow structure into a slow wind ejected during the previous stages of evolution. This frees us from having to use the pressure variation timescale t_P, as defined by KMC94, to constrain a cloud size, since we can set $t_P \to \infty$. On the other hand, for blast waves one cannot assume a steady time-independent postshock flow (for example, supernova remnant blast waves), and the size of the clouds is constrained by the condition $t_{\rm CC} \ll t_P$, as discussed by KMC94. Here $t_{\rm CC}$ is the time necessary for the cloud internal shock to traverse its radius (see eq. [10] for a more rigorous definition).

It should be mentioned that the maximum cloud size is still constrained by the condition of the shock-front planarity. This condition is less restrictive than the one discussed above; however, it still requires a cloud diameter not to exceed 5%–10% of the global shock wave front radius. This condition is satisfied, for example, in the case of the inhomogeneities, or the cometary knots, observed in such planetary nebulae as NGC 2392 and NGC 7293 (e.g., Burkert & O'Dell 1998).

The timescale we use to define time intervals in our numerical experiments is the time required for the incident shock wave to sweep across an individual cloud, called the "shock-crossing time,"

$$t_{\rm SC} = \frac{2a_{\rm max}}{v_S} , \quad (3)$$

where $a_{\rm max} = a_0$ for cloud distributions with identical

[3] In our discussion we assume the perfect gas, i.e., $\gamma = \text{const} = 5/3$ for cloud, intercloud, and postshock material.

[4] This conclusion is true with a restriction that the shock speed v_S is held fixed.

clouds, and $a_{\max} = \max(a_i)$ for cloud distributions of varying size clouds.

Because of the scale-invariance of our simulations, one can, using specific values for the shock velocity and the size of the inhomogeneities, easily convert the time units used in our discussion into physical ones. The parameter t_{SC} is particularly useful in characterizing the problem, since it has clear physical meaning and does not depend on a specific density contrast, which is important in the case of systems containing clouds of different density.

Note that except for the very short period of time when a cloud interacts with the shock front, the former finds itself immersed in a postshock flow or "wind," the pressure and density of which vary only by several percent over the large range of Mach numbers. Since KMC94 showed that the initial interaction with the shock front does not alter the evolution of the system for the varying Mach number, the details of the evolution should not change after the shock front has passed the cloud. Therefore, conclusions about Mach scaling should be valid both for the durations of cloud-wind interactions discussed by KMC94 and for the much longer durations in our experiments.

One final remark should be made concerning the boundary conditions used in our experiments. In all runs we imposed a constant inflow at the left boundary, described by the postshock conditions, which is determined using the Rankine-Hugoniot relations, and open boundary conditions at the right, top, and bottom boundaries. Those outflow boundary conditions were implemented via zero-order extrapolation.

2.3. *Description of the Runs*

All of the runs discussed in this paper contain a Mach 10 shock wave as a part of the initial conditions and embedded clouds with the density contrast of 500. Table 1 presents a summary of our numerical experiments.

In addition to the dependence on the shock Mach number and the cloud density contrast, there are other degrees of freedom present even in the simplest adiabatic case. We considered how the dynamical evolution, e.g., rate of momentum transfer from the shock wave and shock deceleration, mass loading, mixing of cloud material, etc. of the system depend on (1) the number of clouds present in the system, (2) the total cloud mass, (3) the spatial arrangement of clouds, and (4) the individual cloud sizes and masses.

In most of the runs we constrained ourselves to the case of identical clouds, varying only their number and arrangement. Radii of the clouds in all runs except M14$_r$ is 2% of the horizontal extent of the computational domain. In order to simplify consideration of the dependence on a specific cloud arrangement, most runs have a regular cloud distribution, in which the clouds are placed in the vertices of the mesh formed by the centers of the clouds in the run M14. In addition, we considered a more general case of a random cloud distribution with random cloud spatial positions and radii.

All of our numerical experiments were run for about 100 t_{SC}.[5] By this time, each individual cloud has almost completely lost its identity and gained a velocity comparable to the velocity of the global flow. Mixing of cloud material with the global ambient flow is nearly completed by 100 t_{SC} as well.

In order to facilitate our analysis, we track temporal evolution of the global averages and one-dimensional spatial distributions of two quantities, namely (1) the kinetic energy fraction, $\eta_{kin} = E_{kin}/E_{tot}$, and (2) the volume filling factor, ν.

Because of the adiabatic nature of our simulations, the kinetic energy fraction also allows us to track the complementary quantity, the thermal energy fraction $\eta_{term} = E_{term}/E_{tot} = 1 - \eta_{kin}$.

In order to obtain those quantities from the complex data structure of the adaptive mesh simulations, we project the values of the state vector from each grid of the AMR grid hierarchy onto a uniform grid with the resolution of the highest refinement level and that is associated with the computational domain. Such a projection does not cause loss of data or its precision. When this projection is done, we define

[5] For comparison, the experiments considered in KMC94, that have comparable initial cloud–ambient medium density contrast, were run for about 25 t_{SC}.

TABLE 1

SUMMARY OF THE RUNS DISCUSSED

Run	Number of Clouds[a]	Distribution	Number of Rows	x-Spacing	y-Spacing[c]
M1	1	regular	1	...	...
M2	2	regular	1	...	4
A2	2	regular	1	...	12
M3	3	regular	1	...	4
A5	5	regular	1	...	4
M14	14	regular	3	7[b]	4
M14$_r$	14	random	...	6.34[d]	6.34[d]

[a] Total number of clouds present in the system.

[b] Spacing between the centers of clouds in *two different rows*, projected onto the x-axis, in units of the maximum cloud radius $a_{\max}$.

[c] Spacing between the centers of clouds in *the same row*, projected onto the y-axis, in units of the maximum cloud radius $a_{\max}$, except for the run M14$_r$.

[d] Maximum absolute spacing between the cloud centers in *any* direction in the units of the *average cloud radius* for the distribution.

the global averages of the first quantity above as

$$\langle \eta_{\rm kin} \rangle_{\rm 2D} = \frac{\sum_{i=1}^{N_i} \sum_{j=1}^{N_j} \eta_{{\rm kin},ij}}{N_i N_j} \approx \frac{\int_{x_{\rm min}}^{x_{\rm max}} \int_{y_{\rm min}}^{y_{\rm max}} \eta_{\rm kin}(x,y)\, dx\, dy}{(x_{\rm max} - x_{\rm min})(y_{\rm max} - y_{\rm min})}\ , \qquad (4)$$

where N_i and N_j are the numbers of cells of the projected grid in the x- and y-directions, respectively. Such averaging allows us to follow momentum transfer from the shock wave to the system of clouds, in the case of $\langle \eta_{\rm kin} \rangle_{\rm 2D}$, and via the complementary quantity of the global thermal energy fraction $\langle \eta_{\rm term} \rangle_{\rm 2D}$, heating of the cloud system and intercloud material.

We also define the one-dimensional spatial average of that quantity as

$$\langle \eta_{\rm kin} \rangle_{\rm 1D}(x) = \frac{\sum_{j=1}^{N_j} \eta_{{\rm kin},ij}}{N_j} \approx \frac{\int_{y_{\rm min}}^{y_{\rm max}} \eta_{\rm kin}(x,y) dy}{(y_{\rm max} - y_{\rm min})}\ . \qquad (5)$$

Our code follows advection of a passive tracer marking cloud material. In order to follow mixing of the cloud material with the global flow, we define the global average of the volume filling factor $\langle \nu \rangle_{\rm 2D}$ as the ratio of the total number of cells containing cloud material to the total number of cells in the computational domain. We also define the one-dimensional spatially averaged volume filling factor $\langle \nu \rangle_{\rm 1D}$ as the variation with the coordinate x of the ratio of the number of cells containing cloud material in each vertical row of the computational grid to the total number of cells in the vertical dimension.

3. RESULTS

3.1. *General Properties of the Shock-Cloud Interaction*

Figures 2–5 show the time evolution of a shock wave interacting with a single cloud (run M1), three clouds (run M3), 14 identical clouds in the regular distribution (run M14), and 14 clouds of random size in a random distribution (run M14$_r$). Shown are the synthetic Schlieren images of the system at four different times for all four sequences. Each image is obtained by calculating the density gradient at each point,[6] plotted on a gray scale with the white denoting zero and black the maximum density gradient. Every image in each sequence roughly illustrates transitions between the evolutionary phases discussed below.

3.1.1. *Initial Compression Phase*

After the initial contact, an external shock transmits an internal forward shock into a cloud. This causes cloud compression and heating. At the same time, a bow shock forms around the cloud. KMC94 subdivide this phase into two stages: initial transient and shock compression. Our numerical experiments show that, in general, their description is applicable for all cloud distributions except for the cases when individual clouds are almost in contact at time $t = 0$. The cloud interior is dominated by the forward shock wave. In addition, it undergoes further compression because of the ram pressure from the global upstream postshock flow.

[6] To be more precise, the calculated quantity is the gradient of the density logarithm. This makes the images clearer and easier to understand.

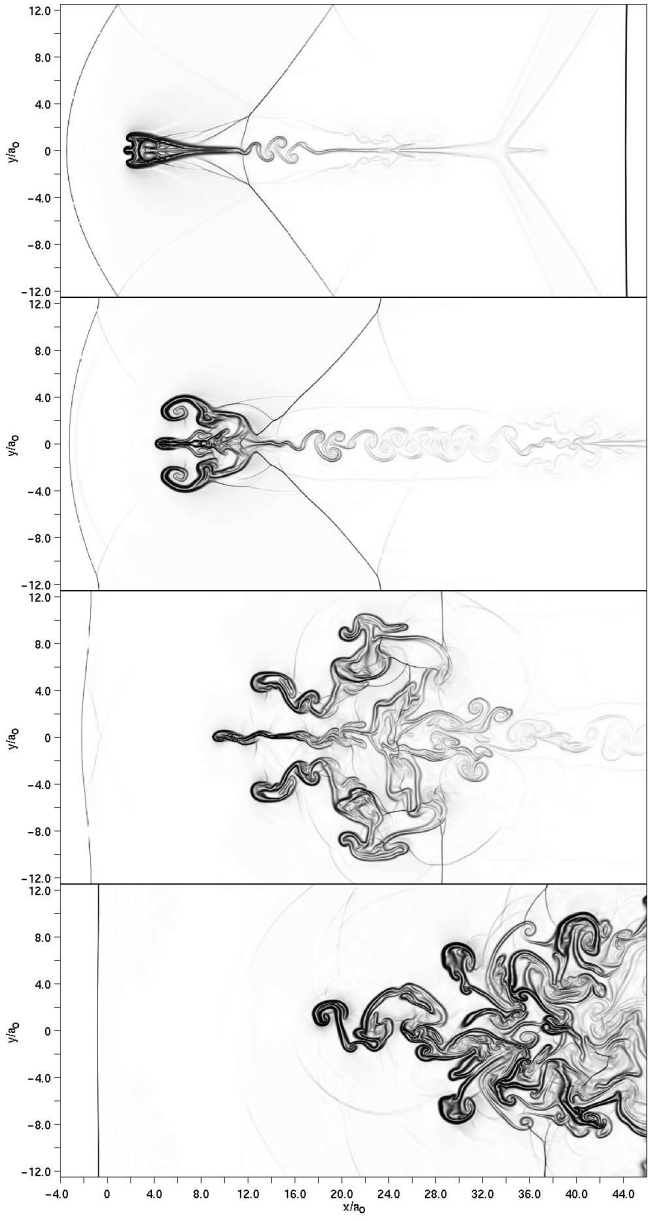

FIG. 2.—Run M1. Time evolution of a system containing a single cloud and interacting with a $M_S = 10$ shock wave. Shown are the synthetic Schlieren images of the system at times $22.47 t_{\rm SC}$, $35.23 t_{\rm SC}$, $50.54 t_{\rm SC}$, and $68.40 t_{\rm SC}$.

A reverse shock forms at the downstream surface of the cloud as a result of the backflow, caused by the global shock convergence behind the cloud. This reverse shock in our simulations never detaches from the downstream surface of the cloud, but instead propagates some small distance upstream (toward the internal forward shock) together with the cloud downstream surface. Moreover, typically the reverse shock is fairly weak, with shock Mach numbers not exceeding 1.2–1.3. This leads to lower maximum densities in the cloud interior reached during this compression phase compared to KMC94; we typically see $\rho_{i,\rm max} \lesssim 6\rho_{i,0}$ as opposed to $\rho_{i,\rm max} \lesssim 10\rho_{i,0}$ quoted by KMC94. The latter value was obtained analytically by KMC94 using the assumption of the collision of two strong shocks, as opposed to the collision of a strong and a weak shock in

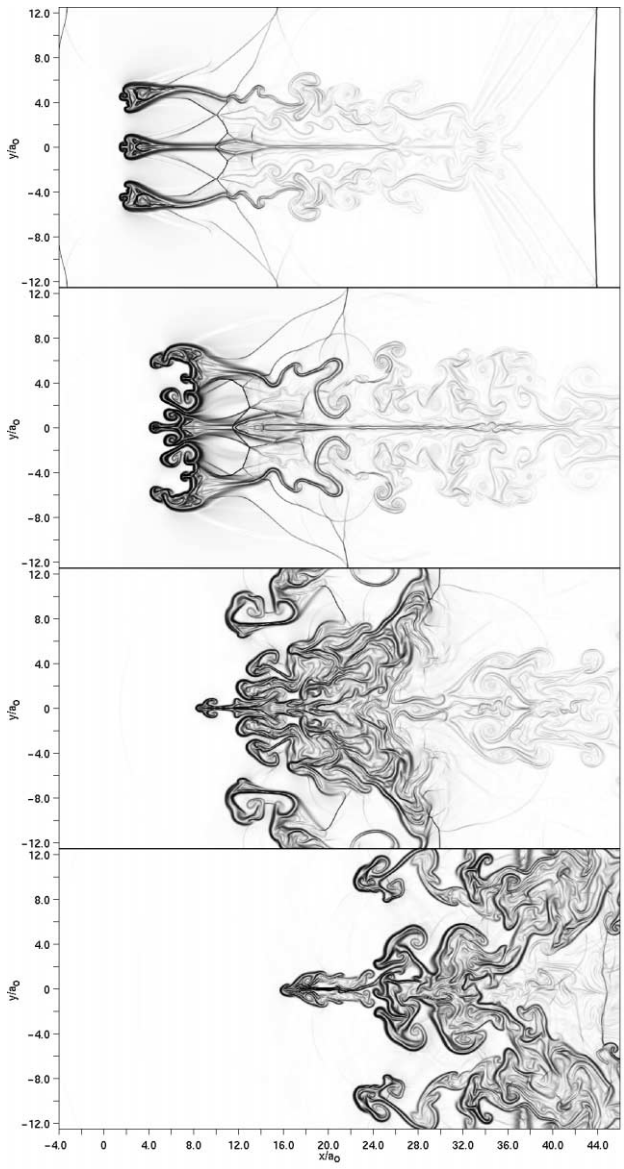

FIG. 3.—Run M3. Time evolution of a system containing three identical clouds and interacting with a $M_S = 10$ shock wave. Shown are the synthetic Schlieren images of the system at times $22.47t_{SC}$, $35.23t_{SC}$, $50.54t_{SC}$, and $68.40t_{SC}$.

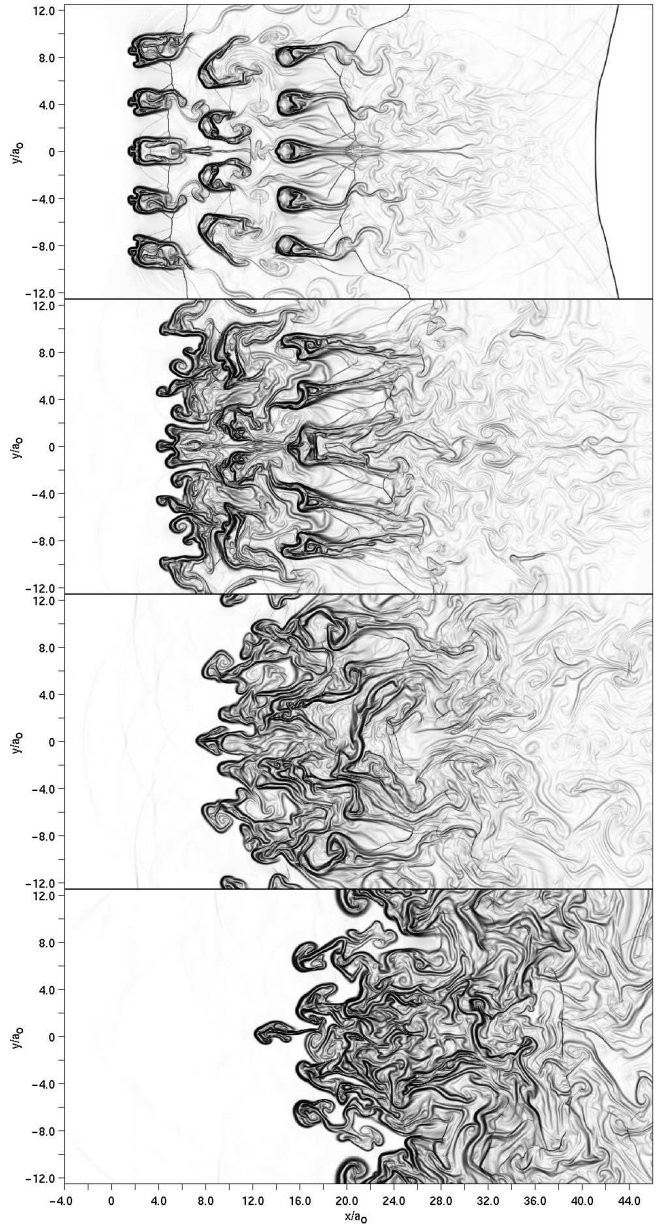

FIG. 4.—Run M14. Time evolution of a system containing 14 identical clouds in a regular distribution and interacting with a $M_S = 10$ shock wave. Shown are the synthetic Schlieren images of the system at times $22.47t_{SC}$, $35.23t_{SC}$, $50.54t_{SC}$, and $69.09t_{SC}$.

reality. Figure 6 illustrates the major flow structures present in the system during the initial compression phase.

Propagation of the forward shock in the cloud allows us to define another important timescale governing the evolution of the system and defining the duration of the compression phase, the "cloud-crushing time," t_{CC}. This is the time necessary for the internal forward shock to cross the cloud and reach its downstream surface,[7]

$$t_{CC} = \frac{2a_{max}}{v_{CS}} \ . \tag{6}$$

In the above expression v_{CS} is the internal forward shock velocity and a_{max} is again defined as a_0 in the cases of cloud distributions with identical clouds, and as $\max(a_i)$ in the cases of cloud distributions with clouds of varying size. Following KMC94, the velocity of the internal forward shock can be written as

$$v_{CS} \simeq \frac{v_S}{\chi^{1/2}} \left(F_{c1} F_{st}\right)^{1/2} , \tag{7}$$

where v_S is the velocity of the external shock. The factor F_{st} relates the external postshock pressure far upstream with the stagnation pressure at the cloud stagnation point and has the form (Klein et al. 1994)

$$F_{st} \simeq 1 + \frac{2.16}{1 + 6.55\chi^{-1/2}} \ . \tag{8}$$

[7] This was the principal timescale in the study of KMC94, although they defined it as the time necessary for the internal forward shock to cross the cloud *radius*. We have changed the definition in our work, since the definition of KMC94 did not actually correspond to the duration of the compression phase. Therefore, t_{CC} in our work is about twice the t_{CC} defined by KMC94.

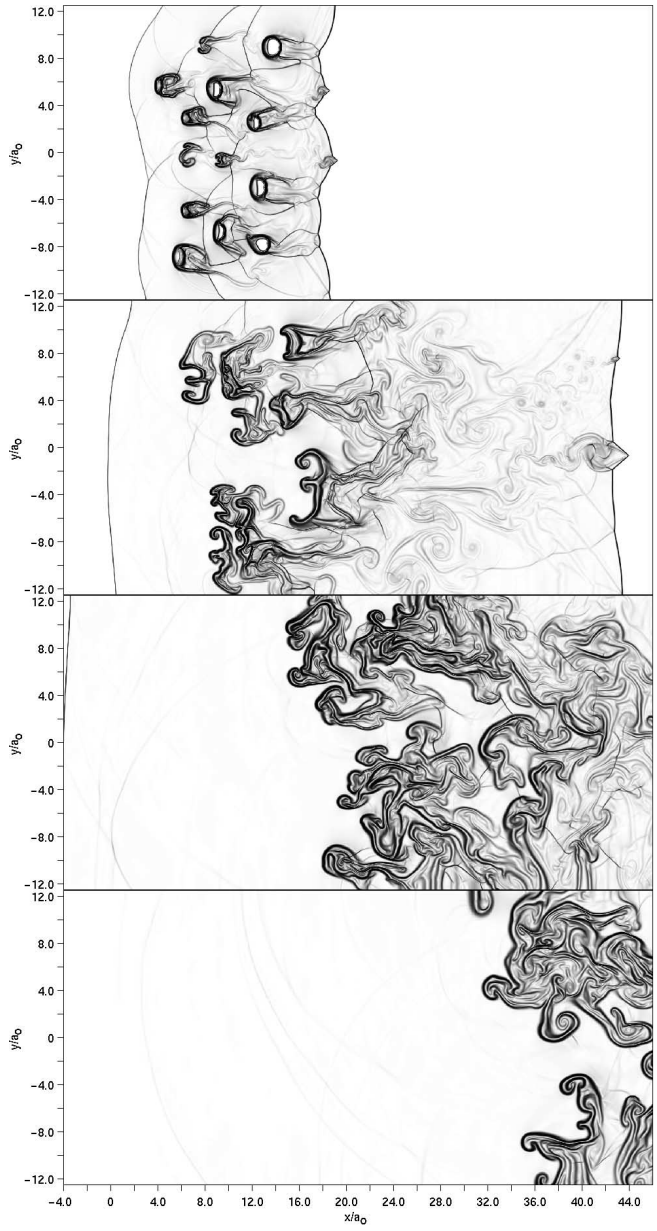

FIG. 5.—Run M14$_r$. Time evolution of a system containing 14 clouds in a random distribution and interacting with a $M_S = 10$ shock wave. Shown are the synthetic Schlieren images of the system at times $9.71t_{SC}$, $22.47t_{SC}$, $45.43t_{SC}$, and $69.09t_{SC}$.

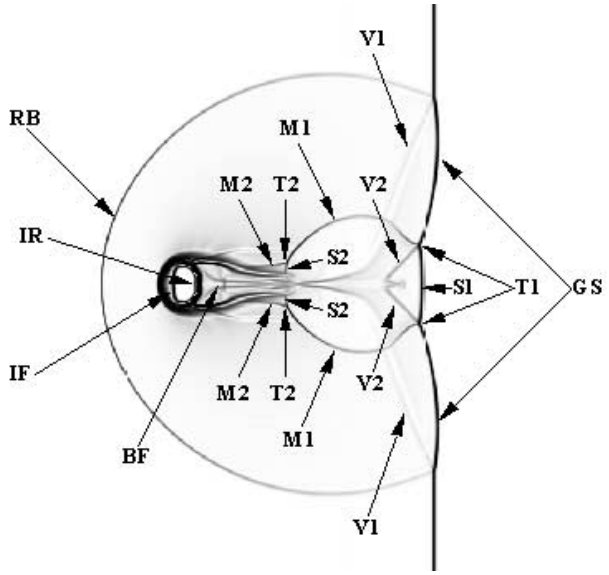

FIG. 6.—Flow structure during the initial compression phase. Shown is the Schlieren image of the run M1 at time $5.1t_{SC}$. GS, external global forward shock; RB, external reverse bow shock; IF, internal forward shock; IR, internal reverse shock; BF, back flow, caused by global forward shock convergence on the symmetry axis; V1, primary vortex sheets, caused by regular reflection of the bow shock; M1, primary Mach reflected shocks, caused by Mach reflection of the global forward shock at the symmetry axis; S1, primary Mach stem (more precisely, two primary Mach stems); T1, primary triple points; V2, secondary vortex sheets, caused by the primary Mach reflection of the global forward shock (note the two stem bulges formed at the base of the secondary vortex sheets near the symmetry axis); M2, secondary Mach reflected shocks; S2, secondary Mach stems; T2, secondary triple points.

The factor F_{c1} relates the stagnation pressure with the pressure just behind the internal forward shock and has an approximate value of 1.3, determined from numerical experiments (Klein et al. 1994).

While we primarily use the shock-crossing time as the major timescale, we occasionally give time in terms of the cloud-crushing time to facilitate comparison with the results discussed by KMC94. For this purpose, we express the cloud-crushing time in terms of the shock-crossing time. Recalling the definition of t_{SC} (eq. [3]), we have

$$t_{CC} = \left[\chi^{1/2}\left(F_{c1}F_{st}\right)^{-1/2}\right] t_{SC} \ . \tag{9}$$

Therefore, for the case of $\chi = 500$,

$$t_{CC} = 12 t_{SC} \ , \tag{10}$$

which agrees to about a few percent with the results of the numerical experiments.

The global properties of the flow at this stage are characterized by the onset of individual bow shocks around each cloud in a time of the order of t_{SC}. By the end of the initial compression phase, those individual bow shocks merge into a single bow shock.[8]

Finally, the downstream flow, i.e., the flow right behind the external forward shock front, is affected by the onset of turbulence in the tails behind the clouds.

[8] It should be noted that a *bow wave* forms instead of a bow shock if the external postshock flow is subsonic, i.e., if

$$M_{PS} = v_{PS}\left(\frac{\gamma P_{PS}}{\rho_{PS}}\right)^{-1/2} \le 1 \ .$$

With the postshock conditions ρ_{PS}, P_{PS}, and v_{PS} determined from the Rankine-Hugoniot relations (Landau & Lifshitz 1959), the above criterion is satisfied for the following values of the external shock Mach number:

$$M_S \le \left(\frac{-\beta + \sqrt{\beta^2 - 4\alpha\delta}}{2\alpha}\right)^{1/2} \approx 2.758 \text{ for } \gamma = \frac{5}{3} \ ,$$

where

$$\alpha = 4 - 2\gamma(\gamma - 1), \ \beta = \gamma^2 - 6\gamma - 7, \ \delta = 2\gamma + 2 \ .$$

Since in this paper we consider the external shocks, Mach numbers of which are typically above 5.0, we hereafter do not consider the possibility of a bow wave formation.

3.1.2. *Re-expansion Phase*

This phase is initiated after the cloud internal forward shock reaches the back of the cloud. Two major processes then occur: lateral expansion of the cloud and the onset of instabilities at its upstream surface. At this stage Rayleigh-Taylor type instabilities dominate at the cloud/ambient flow interface. These are driven in part by the cloud expansion and incipient large-scale fragmentation. The flow downstream with respect to the clouds is dominated by Kelvin-Helmholtz instabilities operating in the growing turbulent region. The combined action of the lateral expansion and the instabilities causes the clouds to take the "umbrella-type" shape and eventually break up.

In the context of those two processes, the initial cloud separation becomes of key importance in defining the subsequent behavior of the whole system. We show below that it can be used to distinguish between the two regimes of cloud evolution, interacting and noninteracting, and can serve as the basis for classification of cloud distributions. In § 3.3 we give a more rigorous discussion of the role of cloud separation. For now we give a qualitative illustration.

Clouds located far enough from each other are not greatly influenced by their neighbors, and their interaction with the flow proceeds independently, as described by KMC94. This case is illustrated in Figure 7. Compared to the evolution of a single cloud system, shown in Figure 2, the two clouds evolve up to the point of their destruction very similarly to the single-cloud case. However, cloud separations can be small enough for the mutual interaction to manifest early during the re-expansion phase, as in Figure 8. This mutual interaction causes changes primarily in the flow between clouds. As a result, the lateral expansion and growth of the Rayleigh-Taylor instabilities in the cloud material is affected. The tails behind the clouds are also deformed outward (see, e.g., also Fig. 3).

The unperturbed supersonic flow that forms behind the external shock wave undergoes a transition from a supersonic to a subsonic regime as it passes through a cloud bow shock. As a consequence, it suffers a significant velocity drop whose magnitude is larger for smaller cloud separations, because of the larger volume of the stagnation zone in front of the clouds. Clouds, acting as de Lavalle nozzles, then cause the flow material to reaccelerate. The flow reaches a sonic point next to a cloud core for the regions of the flow adjacent to a cloud, and farther downstream for the regions of the flow located farther from the clouds. It is important to note that this reacceleration results in rarefaction of the flow and a gradual decrease of both thermodynamic and dynamical pressure. Eventually, as a result of acceleration in the intercloud region, the flow becomes highly supersonic and finally shocks down through a stationary shock formed downstream of the clouds to the regime close to the unperturbed flow behind the external shock (see Figs. 7–8).

From the above discussion it is clear that the lateral expansion velocity depends critically on the cloud separation. For sufficiently low flow speeds, the cloud material will expand at the cloud internal sound speed. With increasing global flow velocities (or, equivalently, with increasing velocities of the external shock front), the lateral expansion velocity will increase as well. This velocity is limited, in principle, by the terminal expansion velocity into vacuum.

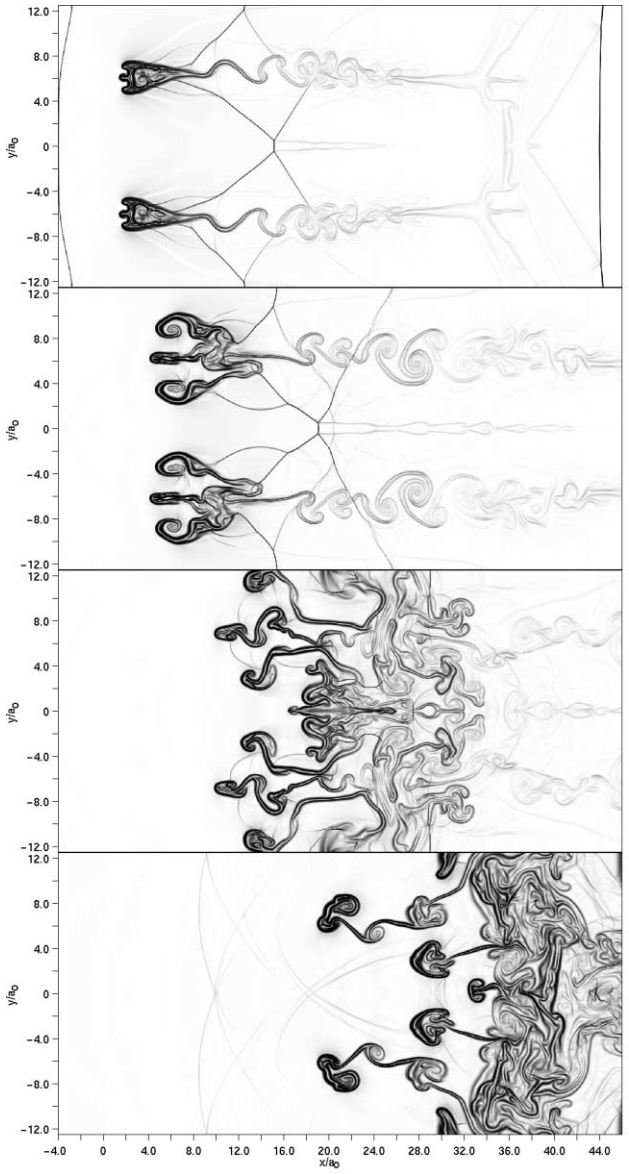

FIG. 7.—Run A2. Illustration of the noninteracting regime of cloud evolution: interaction of a $M_S = 10$ shock wave with a system of two identical clouds with the cloud center separation of $12.0a_0 \approx 2.86d_{\rm crit}$. Shown are the synthetic Schlieren images of the system at times $22.47t_{\rm SC}$, $35.23t_{\rm SC}$, $50.54t_{\rm SC}$, and $68.40t_{\rm SC}$.

For a fixed unperturbed upstream flow, the flow velocity near a cloud lateral surface (facing the space in between the clouds) will be highest in the case of a single cloud or a cloud located far from the neighboring ones. With decreasing cloud separation this velocity will decrease as well, causing higher dynamical pressure on the lateral surface, and therefore lower lateral expansion velocities. This occurs because the velocity drop across a bow shock in the cases of small cloud separations is much larger, because of a stronger stagnation effect in between the bow shock and the clouds. Therefore, flow adjacent to the cloud does not reach velocities as high as in cases of large cloud separations.[9] Another way to look at this process is as follows. The flow adjacent

[9] It should be noted that eventually the velocities reached by the flow downstream after passing the region between clouds are much higher, and consequently the strength of the stationary shock downstream is much larger in the case of small cloud separations.

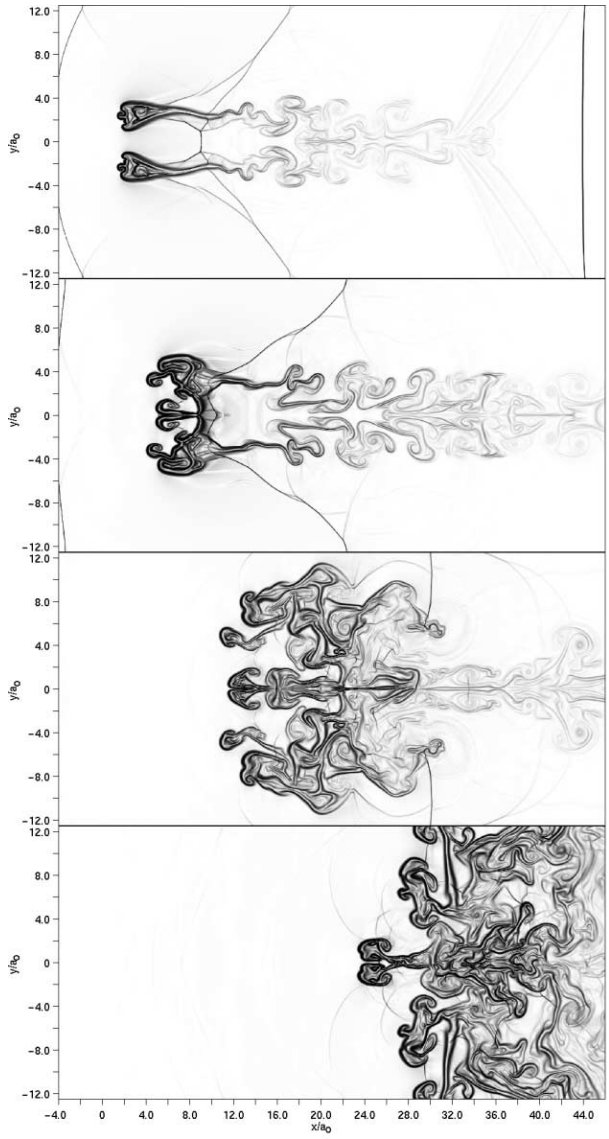

FIG. 8.—Run M2. Illustration of the interacting regime of cloud evolution: interaction of a $M_S = 10$ shock wave with a system of two identical clouds with the cloud center separation of $4.0a_0 \approx 0.95d_{\rm crit}$. Shown are the synthetic Schlieren images of the system at times $22.47t_{\rm SC}$, $35.23t_{\rm SC}$, $50.54t_{\rm SC}$, and $68.40t_{\rm SC}$.

to the cloud surface passes through a sonic point, but in the cases of small cloud separations, densities in the stagnation region are much higher. Thus, flow densities at the sonic point near the cloud lateral surface are much higher. This leads to lower sound speeds, and therefore lower flow speeds.

Following KMC94, the effective lateral expansion velocity $v_{\rm exp}$ can be defined as the internal cloud sound speed,

$$v_{\rm exp} = C_C = v_{\rm CS}\frac{[2\gamma(\gamma-1)]^{1/2}}{\gamma+1}\ , \qquad (11)$$

where $v_{\rm CS}$ is the velocity of the cloud internal forward shock (eq. [7]). Our numerical experiments prove this to be a very good approximation during almost all of the re-expansion phase. The expansion velocity exceeds this value by the end of the re-expansion phase because of stagnation pressure in the regions, formed by the Rayleigh-Taylor instability.

We are now in a position to articulate the temporal evolution of a cloud radius in the direction perpendicular to the upstream flow, $a_\perp(t)$. From the moment of their initial contact with the external shock to the moment of their destruction, the clouds first undergo slight compression in the direction perpendicular to the flow and subsequently re-expand. KMC94's analytic model did not explicitly include cloud compression but instead tried to account for its effect via a reduced monotonic expansion rate from $t = 0$. Since $a_\perp(t)$ is intimately related to the drag exerted on a cloud by the global flow, the theoretical rate of momentum pickup by a cloud (or the rate of cloud deceleration in the reference frame used by KMC94) differed from the numerical result. Namely, in Figure 12*b* of the paper by KMC94 numerical and theoretical results are practically the same up to the time $\approx 2.0t_{\rm CC}$, when the rate of cloud deceleration suddenly increases and the numerical and theoretical results drastically diverge. This moment of time corresponds to the beginning of the re-expansion phase, when the cloud cross section starts to increase, causing an increase of the rate of the momentum transfer from the flow to the cloud. To avoid this problem and simplify an expression for $a_\perp(t)$, we use the following form for evolution of a cloud radius normal to the flow:

$$a_\perp(t) = \begin{cases} a_0 & t \le t_{\rm CC}\ , \\ a_0 + C_C(t - t_{\rm CC}) & t_{\rm CC} \le t \le t_{\rm CD}\ . \end{cases} \qquad (12)$$

Here C_C is given by equation (11), and $t_{\rm CD}$ is the cloud destruction time, defined below in equation (13).

3.1.3. *Cloud Destruction Phase*

Depending on the cloud separation, via the process of re-expansion clouds may come into contact and merge into a single coherent structure. This subsequently interacts with the flow as a whole and eventually breaks up. Thus, for the case of small cloud separations we can define the moment of cloud merging as the onset of the cloud destruction phase. For large cloud separations in which individual clouds get destroyed before ever merging, it is difficult to define the precise onset of the destruction phase, as it may be effectively viewed as a part of the re-expansion phase.

We define the end of the cloud destruction phase as the time at which the largest cloud fragment contains less than 50% of the initial cloud mass. For single-cloud systems or systems of weakly interacting clouds, we define the total time from $t = 0$ until the end of the cloud destruction phase as the "cloud destruction time," $t_{\rm CD}$,

$$t_{\rm CD} = \alpha t_{\rm CC} = \alpha' t_{\rm SC}\ . \qquad (13)$$

Typically $\alpha \approx 2.0$, consistent with KMC94, and using equation (10) we find $\alpha' \approx 24$ in our simulations.

In addition to $t_{\rm CD}$ there is also a cloud system destruction time, $t_{\rm SD}$, which we define as the time when the largest fragment of a cloud located farthest downstream contains less than 50% of its initial mass. For thick-layer systems (to be described later), including strongly interacting cloud distributions, $t_{\rm CD}$ becomes less relevant as a description of the system than $t_{\rm SD}$, because $t_{\rm CD} < t_{\rm SD}$.

3.1.4. *Mixing Phase*

After the end of the destruction phase, the cloud material velocity is still only a small fraction of the global flow veloc-

ity (see eq. [36] below). The velocity difference promotes Kelvin-Helmholtz instabilities at the cloud material–global flow interfaces, and therefore the transition of the system to a turbulent regime. Typically, by the beginning of this phase each cloud has lost its identity as a result of merging with neighboring clouds. As the individual fragments become smaller and the velocity of the global flow relative to the cloud material decreases, Kelvin-Helmholtz instabilities grow faster than the Rayleigh-Taylor–type ones. This eventually results in complete domination by the former of the small-scale fragmentation and causes mixing of cloud material with the flow (Klein et al. 1994).

In our numerical experiments, as can be seen in Figures 2–5, turbulent mixing produces a two-phase filamentary system. The appearance of such a two-phase system results because our code does not include viscous diffusion or thermal conduction, restricting all dissipative effects to numerical diffusion only. The latter acts at the length scales comparable to a cell size at the highest refinement level.

Real dissipative effects also constrain the overall stability of cold dense plasma embedded in a tenuous hotter medium. KMC94 considered the overall effect of thermal conduction on the stability of such two-phase media against evaporation. They concluded that the cloud ablation time due to evaporation, expressed in terms of the shock-crossing time $t_{\rm SC}$, defined in equation (3), has the form

$$t_{\rm ab} = \frac{\chi}{9F(\sigma_0')}\left(\frac{2}{\gamma+1}\right)^{1/2}\left(F_{c1}F_{\rm st}\right)^{-1/2} t_{\rm SC}\ , \qquad (14)$$

where $F(\sigma_0')$ is typically of order unity (Klein et al. 1994). Therefore, for the case of our simulations, the typical ablation time is $t_{\rm ab} \sim 30 t_{\rm SC}$, or comparable to the cloud destruction time.

One can also estimate an effective depth over which diffusion and thermal conduction will disrupt the boundary layer between the two phases over a dynamical timescale, $t_{\rm SC}$. This can be estimated as follows (see Kuncic, Blackman, & Rees 1996 and references therein). For viscous diffusion

$$d_{\rm diff} \sim (D_{\rm diff} t_{\rm SC})^{1/2} = \left(\frac{2}{\sqrt{\gamma}}\frac{a_0}{M_S n_0 \sigma_p}\right)^{1/2}. \qquad (15)$$

Here $D_{\rm diff} = \lambda v_{T,p}$ is the coefficient of viscous diffusion, λ is the effective path length between collisions in the cloud material, $v_{T,p} = (kT_p/m_p)^{1/2}$ is the proton thermal velocity in the ambient postshock gas, $t_{\rm SC}$ is the shock-crossing time, defined by equation (3), n_0 is the initial cloud number density, σ_p is the proton collisional cross section, and M_S is the global shock Mach number. If we assume $n_0 \sim 1000$ cm^{-3}, then for the cases presented in our simulations, $d_{\rm diff}$ is about 1% of the initial cloud radius or, equivalently, is about $\frac{1}{3}$ of a cell of the computational domain at the highest refinement level. For thermal conduction, the effective depth is

$$d_{\rm term} \sim (D_{\rm term} t_{\rm SC})^{1/2} = \left[\frac{2}{\sqrt{\gamma}}\frac{a_0}{M_S n_0 \sigma_p}\left(\frac{m_p}{m_e}\right)^{1/2}\right]^{1/2} = d_{\rm diff}\left(\frac{m_p}{m_e}\right)^{1/4}, \qquad (16)$$

where $D_{\rm term} = \lambda v_{T,e}$ is the thermal diffusion coefficient, λ is again the effective path length between collisions in the cloud material, $v_{T,e} = (kT_e/m_e)^{1/2}$ is the thermal electron velocity in the ambient postshock gas,[10] m_e is the electron mass, and other quantities have the same meaning as in equation (15). Then $d_{\rm term}$ is about 6% of a_0, or equivalently, about twice the size of a computational cell at the highest refinement level. Therefore, should we have included real dissipative effects, they would destroy the smallest resolvable structures over the dynamically relevant timescales. Consequently, any further increase in resolution without providing for appropriate mechanisms able to significantly inhibit diffusion and thermal conduction would not provide additional insights into the real physical evolution of a system.

The importance of the dissipative effects is therefore twofold: on the one hand, for the dynamical stability of small-scale structures and, on the other, for the overall stability of the system as a whole. Consider the stability of the initial system against destruction due to thermal conduction and diffusion. From the arguments given above, dissipative effects prevent survival of the system for any dynamically significant amount of time. As a solution to this problem, KMC94 suggested that weak magnetic fields inhibit thermal conduction and diffusion. Indeed, as shown by Mac Low et al. (1994), evolution of weakly magnetized clouds during the compression and re-expansion phases does not differ significantly from the purely hydrodynamic description. However, the presence of magnetic fields would raise other issues. During the mixing phase the system undergoes transition to turbulence, which may amplify the initially dynamically insignificant magnetic fields. Turbulence can lower values of the plasma parameter $\beta = P_g/P_B$, where P_g is the ideal gas pressure and $P_B = B^2/8\pi$ is the magnetic pressure, to 1 or even smaller values. This may alter the evolution of the system during the later periods of the mixing phase. In this respect only, a fully magnetohydrodynamic study of the evolution of a system of clouds interacting with a strong shock is fully self-consistent (for a series of single cloud MHD studies, see Mac Low et al. 1994; Gregori et al. 1999, 2000; Jones et al. 1996; Miniati et al. 1999; Jun & Jones 1999).

3.2. *Role of Cloud Distribution*

In order to characterize the global properties of the shock/cloud system interaction, we plotted the time evolution of the global quantities defined in § 2.3 for the runs M1, M2, M3, A5, M14, and M14$_r$. Those plots are presented in Figures 9–10.

The important feature of those plots is the striking similarity of the behavior of systems containing similar cloud distributions. The systems containing from one to five clouds arranged in a single layer exhibit exactly the same rate of momentum transfer from the global flow. This is manifested by the linear rates of fractional kinetic energy, $\langle \eta_{\rm kin} \rangle_{\rm 2D}$, increase from $t = 0$ up to $t = 24 t_{\rm SC}$ (see Fig. 9). The value of the slope for those five cases is $0.193 \pm 1.6\%$. The thermal energy, $\langle \eta_{\rm term} \rangle_{\rm 2D}$, behaves complementarily. Such behavior of single-layer systems contrasts with that of the multiple-layer systems, namely, the runs M14 and M14$_r$, which we now discuss.

The two 14 cloud runs have different cloud distributions

[10] We assume that electron temperature and proton temperature are equal, $T_e = T_p$.

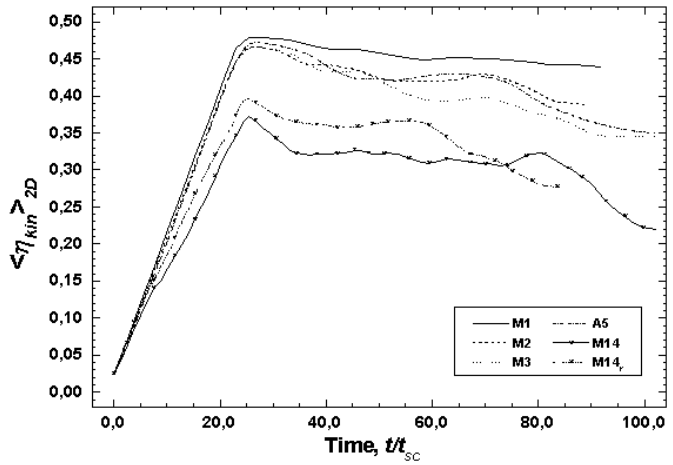

FIG. 9.—Time evolution of the global average of the kinetic energy fraction $\langle \eta_{\rm kin} \rangle_{\rm 2D}$ for the runs M1, M2, M3, A5, M14, and M14$_r$.

(regular as opposed to random), different total cloud mass, and different cloud sizes. Nevertheless, the evolution of their fractional energies is similar. The rate of the kinetic energy increase during compression and re-expansion is the same for both M14 and M14$_r$, and yet is different from that for single-layer cases. The slope in the multilayer cases is also practically constant throughout the two phases, with values of $0.146 \pm 4.5\%$.

Note that for all cases the kinetic (thermal) energy reaches its maximum (minimum) at the time $t = 24t_{\rm SC}$, or the time defined above as the cloud destruction time $t_{\rm CD}$, even though for the 14 cloud runs the cloud system destruction time $t_{\rm SD}$, defined in § 3.1.3, is greater than $t_{\rm CD}$. The fact that the kinetic energy peaks at $t = 24t_{\rm SC}$ signifies that the cloud destruction time is the characteristic timescale for the onset of the fully developed turbulence in the system, which limits the ultimate growth of the kinetic energy fraction. We discuss this in greater detail in § 3.3.2.

After passing through its maximum, the kinetic energy fraction begins to decrease as a result of the transition to turbulence, and consequently turbulent energy dissipation. It is difficult to define a value of the slope for the mixing phase because of the complex nature of the turbulent flow, but the average rate of kinetic energy dissipation in the system is $\approx 0.013 \pm 27\%$ for the single-layer systems and $\approx 0.015 \pm 25\%$ for the multiple-layer ones. The proximity of these two values (within the standard error) is evidence that the systems have lost any unique details of the initial cloud distribution and developed turbulence that depends primarily on the rate of energy input at the largest scale, i.e., on the relative velocity of the global flow with respect to the cloud material.

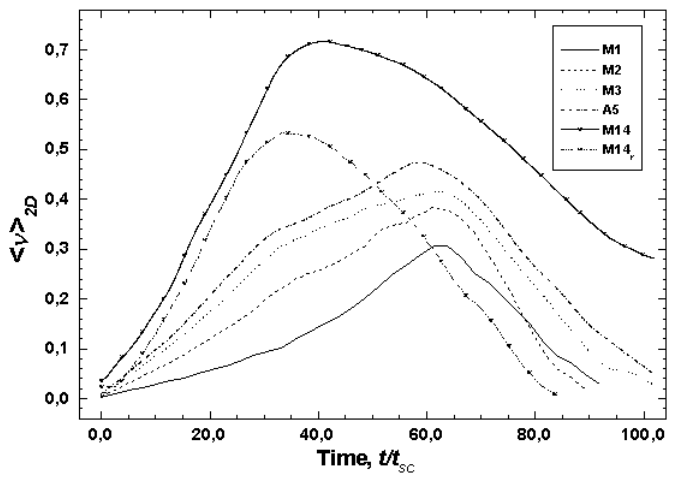

FIG. 10.—Time evolution of the global average of the volume filling factor $\langle \nu \rangle_{\rm 2D}$ for the runs M1, M2, M3, A5, M14, and M14$_r$.

The time evolution of the volume filling factor, $\langle \nu \rangle_{\rm 2D}$, is another example of the similarity in behavior of single- versus multiple-layer systems. As can be seen in Figure 10, the rate of cloud material mixing into the global flow is similar for the single-layer systems but is different from that in multiple-layer ones. The higher mixing rate in the case of multiple-layer distributions results because upstream clouds pick up momentum faster than the downstream ones. Upstream clouds promote destruction of the downstream ones and consequently the overall mixing of the system. The most important feature is that the slopes of the two 14 clump runs, which have different cloud distributions and different total clump mass, from time $t = 0$ to roughly $t = 35t_{\rm SC}$, when they both reach their maximum, is the same, with $d\langle \nu \rangle_{\rm 2D}/dt \approx 0.196 \pm 3.9\%$. In cases of single-layer runs the differences are somewhat greater ($d\langle \nu \rangle_{\rm 2D}/dt \approx 0.067 \pm 25.9\%$). However, this is primarily due to the fact that small numbers of clumps exhibit statistical behavior to a lesser extent, and details of individual clump evolution are more important. With increasing number of clumps, even though the distribution does not change, the slopes become more similar: for the runs M3 and A5, the slope value is $d\langle \nu \rangle_{\rm 2D}/dt \approx 0.078 \pm 7.1\%$. Note that all of the single-layer runs undergo a slight break around $t = 25t_{\rm SC}$, which is associated with clump breakup.[11]

These results lead us to conclude that cloud distribution plays a more important role than the number of clouds or the total cloud mass. We use this conclusion in the next section as the foundation for classifying possible cloud distributions and defining the general type of the cloud system evolution in each category.

3.3. *Critical Density Parameter*

We have seen that the cloud distribution plays the defining role in determining the evolution of a shock-cloud system. We now quantify this statement and define criteria for determining the behavior of a given system.

We define a set of all possible cloud distributions for a given number of clouds N. We consider only the clouds of equal or comparable size and density contrast. We define each set of cloud distributions λ_N for any given number of clouds N to be a set of all possible N pairs of cloud center coordinates satisfying two conditions: (1) each pair of clouds is separated by some minimum distance $r_{\rm min}$, and (2) clouds are confined to a layer extending from the position X_L to the position X_R (see Fig. 1):

$$\forall N \geq 1 : \lambda_N \equiv \left\{ (x_i, y_i), 1 \leq i \leq N : r_{ij} = \left[(x_i - x_j)^2 + (y_i - y_j)^2 \right]^{1/2} \geq r_{\rm min} \approx 2a_0,\ x_i \in [X_L, X_R] \right\} . \quad (17)$$

[11] The presence of the maximum values in $\langle \nu \rangle_{\rm 2D}$ in Figure 10 for all runs is due to the eventual loss of the cloud material through the outflow boundaries.

Next, we consider the complete set of all possible cloud distributions Λ for all possible cloud numbers defined as

$$\Lambda = \bigcup_{N\geq 1} \{\lambda_N\} \ . \tag{18}$$

We define two subsets within this set Λ: a subset of "thin-layer" cloud distributions Λ_I, and a subset of "thick-layer" cloud distributions Λ_M, so that

$$\Lambda_I \cup \Lambda_M = \Lambda \quad \text{and} \quad \Lambda_I \cap \Lambda_M \equiv \emptyset \ . \tag{19}$$

In our numerical experiments those two subsets are associated with the single-row and multiple-row distributions.

In order to give a precise definition of those two fundamental classes of cloud distributions, we need to introduce several auxiliary quantities.

3.3.1. *Cloud Velocity and Displacement*

We now estimate the distance that the cloud material will travel before the cloud breakup, i.e., within the time $t_{\rm CD}$.

The equation of motion of a cloud in the stationary reference frame of the unshocked ambient medium takes the form

$$m_C \frac{dv_C}{dt} = \frac{1}{2} C_D \rho_{\rm PS} (v_{\rm PS} - v_C)^2 A_C(t) \ , \tag{20}$$

where m_C is the mass of the cloud, v_C is the cloud velocity in the stationary reference frame, C_D is the cloud drag coefficient, $\rho_{\rm PS}$ is the undisturbed postshock flow density, and $A_C(t)$ is the cloud cross section area normal to the flow. It should be noted that this equation is valid only until the cloud destruction is complete, i.e., until $t \approx t_{\rm CD}$. From this point on we assume that the drag coefficient $C_D \approx 1$, which is a rather good approximation for a cylindrical body embedded in a supersonic flow of $M_{\rm PS} = 1.31$ (see Klein et al. 1994; Bedogni & Di Fazio 1998; Miller & Bailey 1979).

Let us assume for a moment that the clouds have finite extent in the z-direction, z_0. Note that then

$$m_C = \rho_0 \pi a_0^2 z_0 \ , \tag{21}$$

where ρ_0 is the cloud density and a_0 and z_0 are the cloud dimensions at time $t = 0$. Moreover, the cross section area is

$$A_C(t) = 2 a_\perp(t) z_0 \ , \tag{22}$$

where $a_\perp(t)$ is the cloud radius in the direction normal to the flow. Substituting equations (21) and (22) into equation (20) and using equation (12) for $a_\perp(t)$, we get the modified equation of motion[12]

$$\frac{dv_C}{dt} = \frac{\rho_{\rm PS}}{\rho_0 \pi a_0^2} (v_{\rm PS} - v_C)^2 a_\perp(t) \ . \tag{23}$$

This equation describes motion of the cloud as a result of its interaction with the postshock wind. However, we also need to account for the velocity that the cloud material acquires after its initial contact with the external shock front. This velocity may be comparable to the velocity acquired during the compression and re-expansion phases, and therefore must be carefully taken into consideration.

[12] Note that from now on we omit the cloud drag coefficient, considering it to be equal to 1.

Recall that the initial contact of the incident shock front drives an internal forward shock into the cloud with velocity $v_{\rm CS}$. Cloud material behind the internal shock front gains a velocity $v_{C,\rm PS}$ that can be determined from the Rankine-Hugoniot relations in the usual manner,

$$v_{C,\rm PS} = \frac{2 v_{\rm CS}}{\gamma + 1} \left(1 - \frac{1}{M_{\rm CS}^2} \right) \ . \tag{24}$$

Here $M_{\rm CS}$ is the Mach number of the cloud internal forward shock, which can be expressed in terms of the external shock Mach number as

$$M_{\rm CS} = \frac{v_{\rm CS}}{C_{C,0}} = M_S \left(F_{c1} F_{\rm st} \right)^{1/2} \ , \tag{25}$$

where $C_{C,0}$ denotes the sound speed in the unshocked cloud material, and we have used equation (7) for $v_{\rm CS}$. For the simulations discussed in this paper ($\chi = 500$ and $\gamma = 5/3$), the internal cloud shock Mach number is $M_{\rm CS} = 1.86 M_S = 18.6$.

Substituting equation (7) for $v_{\rm CS}$ and equation (25) for $M_{\rm CS}$ into equation (24), and expressing the external shock velocity v_S in terms of the unperturbed upstream postshock velocity $v_{\rm PS}$, we obtain the following expression for the velocity of the cloud material due to the cloud interaction with the external shock front:

$$v_{C,\rm PS} = v_{\rm PS} \left\{ \frac{\left(F_{c1} F_{\rm st} \right)^{1/2} \left[M_S^2 - \left(F_{c1} F_{\rm st} \right)^{-1} \right]}{\chi^{1/2} \left(M_S^2 - 1 \right)} \right\} = v_{\rm PS} \Gamma \ . \tag{26}$$

For the case of $M_S = 10$, $\Gamma = 0.084$. Note that for the limiting case $M_S \rightarrow \infty$, the value of Γ remains practically unchanged at 0.083, which corroborates the previously discussed Mach scaling.

Finally, making use of the fact that the relative velocity of the postshock flow with respect to the cloud is now $(v_{\rm PS} - v_{C,\rm PS} - v_C)$, we can integrate equation (23) and obtain the following form of the cloud velocity:

$$v_C(t) = \begin{cases} v_{\rm PS} \left[1 - \dfrac{1}{At + (1 - \Gamma)^{-1}} \right] & t \leq t_{\rm CC} \ , \\ v_{\rm PS} \Big\{ 1 - [AB(t - t_{\rm CC})^2 & \\ \quad + A(t - t_{\rm CC}) + C]^{-1} \Big\} & t_{\rm CC} \leq t \leq t_{\rm CD} \ , \end{cases} \tag{27}$$

where we introduced the quantities

$$A = \frac{\rho_{\rm PS} v_{\rm PS}}{\rho_0 \pi a_0} = \frac{1}{t_{\rm SC} \chi} \left\{ \frac{\pi}{2} \left[\frac{2}{\gamma + 1} \left(1 - \frac{1}{M_S^2} \right) \right]^{-1} - 1 \right\}^{-1} \ , \tag{28}$$

$$B = \frac{C_C}{2 a_0} = \frac{1}{t_{\rm SC} \chi^{1/2}} \left(F_{c1} F_{\rm st} \right)^{1/2} \left[\frac{3\gamma(\gamma - 1)}{4(\gamma + 1)} \right]^{1/2} \ , \tag{29}$$

$$C = 12 A t_{\rm SC} + (1 - \Gamma)^{-1} \ . \tag{30}$$

The unperturbed postshock quantities $\rho_{\rm PS}$ and $v_{\rm PS}$ are determined from the Rankine-Hugoniot conditions (Landau & Lifshitz 1959), C_c is the sound speed in the shocked cloud, defined by equation (11), and the factor $F_{\rm st}$ is defined by the relation given in equation (8).

The first quantity, A, relates the specific momentum of the postshock wind to the cloud inertia (mass). Thus, it

defines the rate of the momentum pickup by a cloud during the compression phase, when the cloud dimension transverse to the flow does not increase. The second quantity, B, is the inverse sound crossing time in a compressed cloud, i.e., at the end of the compression phase, again for the cloud dimension transverse to the flow. This quantity determines the rate of the cloud lateral expansion. Therefore, during the re-expansion phase the regular momentum transfer from the wind to the cloud, described by A, is augmented by the cloud lateral expansion, described by B, which comes as an additional factor in the quadratic dependence on t. The quantity C ensures continuity of the cloud velocity during the transition from the compression to the re-expansion phase.

Next, integrating equation (27) from time $t = 0.0$ up to the cloud destruction time $t = t_{\rm CD}$, we can determine the displacement of cloud material during the compression and re-expansion phases,

$$L_C(t) = \begin{cases} v_{\rm PS}\left\{t - \dfrac{1}{A}\ln[(1-\Gamma)At + 1]\right\} & 0 \le t \le t_{\rm CC}\ , \\ v_{\rm PS}\left(t - \dfrac{1}{A}\left\{\dfrac{2}{q}\tan^{-1}\dfrac{(t-t_{\rm CC})q}{(t-t_{\rm CC}) + 2C/A}\right.\right. & \\ \quad \left.\left. + \ln[(1-\Gamma)At_{\rm CC} + 1]\right\}\right) & t_{\rm CC} \le t \le t_{\rm CD}\ , \end{cases} \tag{31}$$

where $q = (4BC/A - 1)^{1/2}$. This allows us to estimate the total displacement a cloud incurs before its destruction, called the "cloud destruction length,"

$$L_{\rm CD} = L_C(t_{\rm CD})\ . \tag{32}$$

In order to get a clearer understanding of the general equations (27) and (31), let us consider two cases: the case presented in our simulations with $M_S = 10$, and the limiting case of $M_S \to \infty$. We assume in both cases a density contrast of $\chi = 500.0$ and $\gamma = 5/3$.

First, we rewrite equation (27) as

$$v_C(t) = \begin{cases} v_{\rm PS}\left[1 - \left(\dfrac{t}{t_{\rm SC}}a_1 + a_2\right)^{-1}\right] & t \le t_{\rm CC}\ , \\ v_{\rm PS}\left\{1 - \left[\left(\dfrac{t}{t_{\rm SC}} - 12\right)^2 b_1\right.\right. & \\ \quad \left.\left. + \dfrac{t}{t_{\rm SC}}a_1 + a_2\right]^{-1}\right\} & t_{\rm CC} \le t \le t_{\rm CD}\ . \end{cases} \tag{33}$$

In the first case of $M_S = 10$, the coefficients a_1, a_2, and b_1 have the values

$$a_1 = 1.79 \times 10^{-3}\ , \quad a_2 = 1.09, \quad b_1 = 8.35 \times 10^{-5}\ . \tag{34}$$

Substituting these into equation (33), we find that at the end of the compression phase, i.e., at the time $t = 12t_{\rm SC}$, the cloud velocity is 10% of the postshock velocity $v_{\rm PS}$ and 7.5% of the shock velocity v_S. On the other hand, at the end of the re-expansion phase, i.e., at the time $t = 24t_{\rm SC}$, the cloud velocity is 12.66% of $v_{\rm PS}$ and 9.4% of v_S.

For the case $M_S \to \infty$, the above coefficients have the values[13]

$$a_1 = 1.83 \times 10^{-3}\ , \quad a_2 = 1.09\ , \quad b_1 = 8.51 \times 10^{-5}\ . \tag{35}$$

Substitution into equation (33) gives us the maximum values of the velocity that a cloud can reach in the case of an infinitely strong shock:

$$\begin{aligned} v_{C,\max} &= 10.1 \times 10^{-2} v_{\rm PS} = 7.55 \times 10^{-2} v_S \\ &\quad \text{for the compression phase}\ , \\ v_{C,\max} &= 12.8 \times 10^{-2} v_{\rm PS} = 9.57 \times 10^{-2} v_S \\ &\quad \text{for the re-expansion phase}\ . \end{aligned} \tag{36}$$

Similarly, we can determine the values of cloud displacement for the two cases considered above. Equation (31) for L_C can be rewritten as

$$L_C(t) = \begin{cases} a_0 c_1\left\{\dfrac{t}{t_{\rm SC}} - \dfrac{1}{a_1}\ln\left[\dfrac{t}{t_{\rm SC}}\left(\dfrac{a_1}{a_2}\right) + 1\right]\right\} & 0 \le t \le t_{\rm CC}\ , \\ a_0 c_1\left[\dfrac{t}{t_{\rm SC}}\right. & \\ \quad \left. - c_2\tan^{-1}\left(\dfrac{t/t_{\rm SC} - 12}{t/t_{\rm SC}c_4 + c_5}\right) - c_3\right] & t_{\rm CC} \le t \le t_{\rm CD}\ , \end{cases} \tag{37}$$

where for the case $M_S = 10$ the coefficients a_1 and a_2 have the values defined in equation (34), and for $M_S \to \infty$ the values defined in equation (35).

In the case $M_S = 10$ the coefficients c_1, c_2, c_3, c_4, and c_5 have the values

$$c_1 = 1.49\ , \quad c_2 = 104.17\ , \quad c_3 = 10.89\ , \quad c_4 = 9.34 \times 10^{-2}\ , \quad c_5 = 113.72\ .$$

Substitution into equation (37) gives us the displacement that the cloud material undergoes by the end of the compression and re-expansion phases: $1.6a_0$ and $3.5a_0$, respectively.

In the limiting case $M_S \to \infty$, the values of the coefficients c_1, c_2, c_3, c_4, and c_5 are

$$c_1 = 1.5\ , \quad c_2 = 103.22\ , \quad c_3 = 10.9\ , \quad c_4 = 9.43 \times 10^{-2}\ , \quad c_5 = 112.56\ .$$

Substituting these coefficients into equation (37) we find that by the end of the compression phase the cloud is displaced by the distance of $1.65a_0$, whereas by the end of the re-expansion phase the displacement is $3.53a_0$.

It is clear from the results obtained above that both the velocity and cloud displacement values in the case $M_S = 10$ are practically identical to the maximum values achieved in the limiting case of $M_S \to \infty$. Therefore, our results obtained for the case of a Mach 10 shock can be considered as the limiting ones for the cases of strong shocks.

These results, derived for single clouds or systems with large separation, are in good agreement with numerical

[13] Note that the assumption here is the same as in the discussion of Mach scaling, namely, while increasing the shock Mach number, we keep the shock front velocity in the stationary reference frame constant.

experiments. Typically, the maximum difference between numerical and analytical values of cloud velocity and position never exceeds 10%. The analytical results are usually an overestimate of the numerical ones. This is due to a slight overestimation of the initial velocity gain after the contact with the external shock front and because we assumed the cloud cross section to be constant during the compression phase, whereas it undergoes a small decrease in the experiments.

Therefore, the maximum distance a cloud with a density contrast of 500 can travel before its destruction after the initial interaction with a strong shock is

$$L_{\rm CD,max} \approx 3.5 a_0 \ . \tag{38}$$

Finally, it should be noted that the values of the maximum cloud velocity at the moment of breakup, $v_{C,\rm max}$, given in equation (36), and the maximum cloud destruction length, $L_{\rm CD,max}$, given in equation (38), are still functions of the cloud–ambient medium density contrast χ. Therefore, for a different value of χ the values of $v_{C,\rm max}$ and $L_{\rm CD,max}$ should be determined by direct evaluation of equations (27) and (31).[14] Although the change in $v_{C,\rm max}$ can be quite significant, we find that $L_{\rm CD,max}$ does not change so prominently with varying χ. For example, for $\chi = 40.0$, which is more than an order of magnitude less than the value $\chi = 500.0$ used above, $v_{C,\rm max} = 36.5 \times 10^{-2} v_{\rm PS}$, which is almost 3 times the value given in equation (36). However, the corresponding value of $L_{\rm CD,max} \approx 3.54 a_0$, which is only a 1% increase compared to the value in equation (38). This is due to the fact that clouds with lower density accelerate faster, although their destruction time is shorter. Therefore, even though the value of the cloud velocity at the time of breakup should be evaluated for each particular value of χ, the cloud destruction length value given in equation (38) can be used with a sufficiently high accuracy over the full range of density contrasts considered in this work, i.e., $\chi = 10$–1000.

3.3.2. *Critical Cloud Separation*

We first define the average cloud separation between a clump and its nearest neighbor, projected on to the direction of the flow, $\langle \Delta x_N \rangle$, and perpendicular to it, $\langle \Delta y_N \rangle$, for a given cloud distribution,

$$\langle \Delta x_N \rangle = \frac{1}{N} \sum_{i=1}^{N} \min_{j \in [1,N]} \{ |x_i - x_j| \} \ , \tag{39}$$

$$\langle \Delta y_N \rangle = \frac{1}{N} \sum_{i=1}^{N} \min_{j \in [1,N]} \{ |y_i - y_j| \} \ . \tag{40}$$

We can also define a maximum cloud separation projected onto the direction of the flow, or the "cloud layer thickness,"

$$(\Delta x_N)_{\rm max} = \max_{i,j \in [1,N]} \{ |x_i - x_j| \} \ . \tag{41}$$

Now we are in a position to give a precise definition of the "thin-layer" and "thick-layer" systems. We define a distribution of clouds to belong to the subset Λ_I if its maximum cloud separation $(\Delta x_N)_{\rm max}$ does not exceed the cloud destruction length, $L_{\rm CD}$. The distribution belongs to the subset Λ_M in all other cases:

$$\begin{aligned} \Lambda_I &\equiv \{ \lambda_N : (\Delta x_N)_{\rm max} \le L_{\rm CD} \} \ , \\ \Lambda_M &\equiv \{ \lambda_N : (\Delta x_N)_{\rm max} > L_{\rm CD} \} \ . \end{aligned} \tag{42}$$

A more intuitive way to look at this classification is as follows. As we have seen, a cloud interacting with the postshock flow re-expands and breaks up before it proceeds into the mixing phase. The above criterion tells us if any cloud or a row of clouds will complete its destruction phase prior to encountering any other clouds located downstream. The definition (42) appears to rather accurately draw the line between cloud systems of two types.

In practice, the maximum cloud separation $(\Delta x_N)_{\rm max}$ (eq. [41]) is simply the thickness of the layer of inhomogeneities in a real system and should be compared to the cloud destruction length. This thickness can be obtained from the observations of a particular object, or it can be found analytically, e.g., via consideration of instabilities at the interface between two flows.

Having defined the two classes, or subsets, of cloud distributions, we now consider the behavior of the clouds in each class. First we consider Λ_I, the "single-row" distributions. On average, by the time the clouds are displaced by the distance $L_{\rm CD}$, all of them will be destroyed and will proceed to the mixing phase. Thus, the time of the destruction should be approximately $t_{\rm CD} \simeq t_{\rm SD}$.

The question arises whether clouds will interact during the process of re-expansion and destruction. We can give a formal criterion for this. Consider two clouds with separation $\langle \Delta y_N \rangle = d$ and $(\Delta x_N)_{\rm max} \le L_{\rm CD}$. Both clouds will expand laterally at the velocity $v_{\rm exp}$ defined by equation (11). Consequently, the time for the clouds to come into contact is

$$t_{\rm merge} \approx \frac{d - 2a_0}{2 v_{\rm exp}} \ . \tag{43}$$

Such re-expansion starts after the cloud compression phase, i.e., after the time $t_{\rm CC}$, and cannot proceed beyond the cloud destruction time $t_{\rm CD}$. Therefore, setting $t_{\rm merge} = t_{\rm CD} - t_{\rm CC}$, we find the following critical cloud separation transverse to the global flow:

$$d_{\rm crit} = 2 \left[a_0 + v_{\rm exp} (t_{\rm CD} - t_{\rm CC}) \right] \ . \tag{44}$$

Substituting equation (11) explicitly for the expansion velocity and equation (13) for the cloud destruction time into the equation (44), we obtain

$$d_{\rm crit} = 2 a_0 \left\{ \frac{t_{\rm CD} - t_{\rm CC}}{t_{\rm SC}} \left(\frac{F_{c1} F_{\rm st}}{\chi} \right)^{1/2} \left[\frac{3\gamma(\gamma - 1)}{\gamma + 1} \right]^{1/2} + 1 \right\} . \tag{45}$$

In other words clouds whose separation transverse to the flow is less than $d_{\rm crit}$ will come into contact and merge before their destruction is completed. Therefore, their evolution during the destruction phase (and for the most part of the re-expansion phase) cannot be considered as the evolution of two independent clouds.

The critical separation does not depend on the global shock Mach number, which is consistent with the Mach scaling, discussed above. Therefore, this parameter is

[14] Note that dependence on χ also comes via the cloud destruction time $t_{\rm CD}$, which should be substituted into eqs. (27) and (31).

universal for all strong shocks and for all possible distributions from the subset Λ_I. For the case $\gamma = 5/3$ and $\chi = 500$, we find the critical cloud separation to be approximately

$$d_{\rm crit} \approx 4.2 a_0 \ . \tag{46}$$

For cloud distributions from the subset Λ_I that have an average separation $\langle \Delta y_N \rangle \gg d_{\rm crit}$, the evolution of the system will proceed in the noninteracting regime. On the other hand, for the distributions for which $\langle \Delta y_N \rangle \lesssim d_{\rm crit}$, the cloud-cloud interactions are important throughout the reexpansion and destruction phases, placing them in an interacting regime.

It is more difficult to formulate a unified criterion for the behavior of the systems in the class Λ_M. When $\langle \Delta x_N \rangle > L_{\rm CD}$, such systems can be considered as a set of thin layers with an average separation greater than $L_{\rm CD}$, i.e., each row can be considered as a system from the subset Λ_I. Consider, for example, the run M_{14}, presented in Figure 4. From Table 1, the average separation $\langle \Delta x_N \rangle$ for this run is equal to 7, i.e., $\langle \Delta x_N \rangle > L_{\rm CD}$. Indeed, the evolution of the leftmost row of clouds proceeds as a simple single-row case, and its destruction is completed by the time $t_{\rm CD}$. This results in the fractional kinetic energy reaching a maximum at the time $t_{\rm CD} \approx 24 t_{\rm SC}$ (see Fig. 9). However, it is clear from Figure 4 that the evolution of the downstream rows is altered by the destruction of the leftmost one. Therefore, when $\langle \Delta x_N \rangle > L_{\rm CD}$ one must account for the fact that the destruction of an upstream layer of clouds will change the properties of the global flow for the next, downstream layer. The new averaged values of the velocity, density, and pressure in the global flow should then be used as an input for the analysis of the downstream cloud layer.

3.4. *Mass Loading*

One of the principal questions concerning the effects of shock/cloud-system interactions is the role of mass loading (Hartquist & Dyson 1988). Mass loading is defined as the feeding of material into the global flow by nearly stationary clouds. Analytical studies have predicted a number of important changes when mass loading occurs. The most important of these is the transition of the flow to a transonic regime (Hartquist et al. 1986; Hartquist & Dyson 1988; Dyson & Hartquist 1992, 1994). In our numerical experiments we consider whether mass loading indeed is prominent.

Mass loading can occur only from time $t = 0$ up to the moment of cloud destruction at time $t = t_{\rm CD}$. In our experiments the cloud destruction time is fairly short compared to the total age of most relevant astrophysical objects. Indeed, cloud destruction is practically completed by the time the shock wave reaches the right boundary of the computational domain, i.e., by the time the shock wave travels the distance of about 20–30 cloud sizes. This could, for example, be compared with clump systems in planetary nebulae (PNs). Assuming typical size for PNs clouds to be about 100 AU (which is the size of cometary knots in NGC 7293; Burkert & O'Dell 1998), a density contrast of 500, and a shock wave velocity of 100 km s^{-1}, we find that clouds get completely destroyed within approximately 100–150 yr. This is much less than the typical age of the PN (10^4–10^5 yr).

Thus, clouds with low density contrast, $\chi_i \approx 10$–100, cannot provide significant mass loading because of the ease with which they are advected and destroyed by the global flow. On the other hand, clouds with higher density contrasts, $\chi_i > 100$, retain their low velocities with respect to the global flow for much longer periods of time, and therefore may potentially be efficient mass-loading sources. However, it should be noted that this higher relative velocity of a cloud increases the efficiency of the instability formation, thereby promoting cloud destruction and its mixing with the flow.

We can also consider the amount of mass seeded into the flow, i.e., stripped off from the clouds and assimilated into the global flow, before cloud destruction. Typically, in our experiments the amount of seeded cloud material does not exceed a few percent of the total cloud mass, which is unlikely to be enough to switch the flow into a mass-loaded regime. Figure 11 shows the distribution of cloud material along the direction of the flow or, to be more precise, the distribution of the parameter $\langle \nu \rangle_{\rm 1D}(x)$ for the three-cloud run M3. There the clouds have the separation $\langle \Delta y_N \rangle \approx 0.95 d_{\rm crit}$. The first graph corresponds to the end of the compression phase, while the second corresponds to the end of the destruction phase. The graphs show that cloud material remains localized in the vicinity of the cloud cores until the moment of cloud destruction, and the system does not exhibit any significant mass loading. Moreover, the graphs 3 and 4 of Figure 11, showing cloud material distribution early in the mixing phase, indicate that even after destruction cloud material remains localized within the region of about 8 cloud radii and retains almost the same average velocity with respect to the global flow. Only further on in the mixing phase does cloud material spread significantly.

In conclusion, we can say that for the cloud density contrast values in the range $\chi_i \approx 10$–1000 and practically all values of the global shock wave Mach number, the flows are not likely to be subject to mass loading. This is due to the fact that such relatively low density clumps on one hand accelerate rather rapidly, and on the other fairly quickly become destroyed by instabilities. These flows will be dominated by the mixing of cloud material with the global flow that occurs after cloud destruction. Systems with very dense clouds, $\chi_i \gg 1000$, may provide sites suitable for mass loading. Future numerical studies are required to verify this.

4. CONCLUSIONS

We have numerically investigated the interaction of a strong, planar shock wave with a system of inhomogeneities. These "clumps" are considered to be infinitely long cylinders embedded in a tenuous, cold ambient medium. We have assumed constant conditions in the global postshock flow, thereby constraining the maximum size of the clouds only by the condition of the shock front planarity. Our results are applicable to strong global shocks with Mach numbers $3 \lesssim M_S \lesssim 1000$. The range of the applicable cloud/ambient density contrast values is 10–1000.

We considered four major phases of the cloud evolution due to the interaction of the global shock and postshock flow with a system of clouds. These are: initial compression phase, re-expansion phase, destruction phase, and mixing phase. We describe a simple model for the cloud acceleration during the first three phases, i.e., prior to its destruction, and derive expressions for the cloud velocity and displacement. The results of that model are in excellent agreement with the numerical experiments. The difference in the values of cloud velocity and displacement between

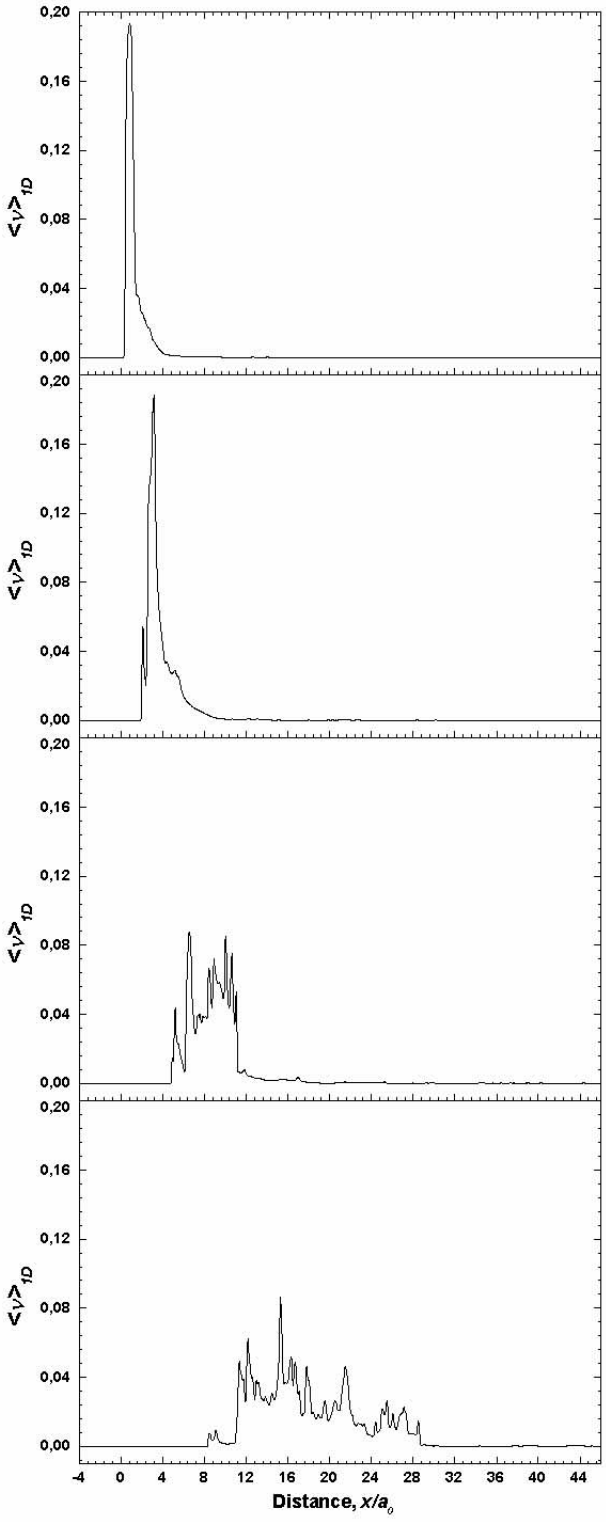

FIG. 11.—Distribution of cloud material along the horizontal dimension of the computational domain for the run M3. Shown are the one-dimensional spatial averages of the volume filling factor $\langle \nu \rangle_{1D}$ at times $12.26t_{SC}$, $25.02t_{SC}$, $37.78t_{SC}$, and $50.54t_{SC}$.

analytical and numerical results is $\lesssim 10\%$. The maximum cloud displacement due to its interaction with a strong shock (prior to its destruction) does not exceed 3.5 initial maximum cloud radii. The maximum cloud velocity is not more than 10% of the global shock velocity.

The principal conclusion of the present work is that the set Λ of all possible cloud distributions can be subdivided into two large subsets, Λ_I and Λ_M. The first subset is Λ_I, thin-layer systems. This subset is defined by the condition that the maximum cloud separation along the direction of flow, or the cloud layer thickness, is not greater than the cloud destruction length, $(\Delta x_N)_{\max} \leq L_{CD}$. The thick-layer systems, Λ_M, are defined by the condition $(\Delta x_N)_{\max} > L_{CD}$. The evolution of cloud distributions within each subset exhibit striking similarity in behavior. We conclude that the evolution of a system of clouds interacting with a strong shock depends primarily on the total thickness of the cloud layer and the cloud distribution in it, as opposed to the total number of clouds or the total cloud mass present in the system. The key parameters determining the type of cloud system evolution are therefore the critical cloud separation transverse to the flow, d_{crit} (this is also the critical linear cloud density in the layer), and the cloud destruction length, L_{CD}.

For a given astrophysical situation, our results indicate that one might determine, either from observations or from theoretical analysis, the thickness of the cloud layer $(\Delta x_N)_{\max}$. This will then determine the class of the given cloud distribution, Λ_I or Λ_M. For cloud distributions from the set Λ_I with average cloud separation $\langle \Delta y_N \rangle > d_{crit}$, evolution of the clouds during the compression, re-expansion, and destruction phases will proceed in the noninteracting regime, and the formalism for a single-cloud interaction with a shock wave (e.g., Klein et al. 1994; Jones et al. 1996; Mac Low et al. 1994; Lim & Raga 1999) can be used to describe the system. On the other hand, if the cloud separation is less than the critical distance, the clouds in the layer will merge into a single structure before their destruction is completed. Although throughout the compression phase they can still be considered independently of each other, their evolution during the re-expansion and destruction phases clearly proceeds in the interacting regime.

When the distribution belongs to the subset Λ_M, it is necessary to determine the average cloud separation projected onto the direction of the flow $\langle \Delta x_N \rangle$, defined by equation (39), and compare it to L_{CD}: if $\langle \Delta x_N \rangle > L_{CD}$, evolution of the cloud system can be roughly approximated as the evolution of a set of distributions from the subset Λ_I, and the above "thin-layer case" analysis applies. If, on the other hand, $\langle \Delta x_N \rangle \leq L_{CD}$ (especially if $\langle \Delta y_N \rangle < d_{crit}$), the system evolution is dominated by cloud interactions, and a thin-layer formalism is inappropriate.

Finally, we have considered the role of mass loading. Here our principal conclusion is that the mass loading is not significant in the cases of strong shocks interacting with a system of inhomogeneities for density contrasts in the range 10–1000. In part this is due to short survival times of clouds under such conditions, and in part it is due to the very low mass-loss rates of the clouds even during the times prior to their destruction. Mass loading may well be important in higher density clouds (Dyson & Hartquist 1994).

The major limitation of our current work is the purely hydrodynamic nature of our analysis, which does not include any consideration of magnetic fields. As discussed in § 3.1.4, cold dense inhomogeneities (clouds) embedded in tenuous hotter medium are inherently unstable against the dissipative action of diffusion and thermal conduction. This evaporates the clouds on the timescales comparable to, or shorter than, the timescales of the dynamical evolution of the system. It was suggested that the magnetic fields may play a stabilizing role against the action of the dissipative

mechanisms. Although weak magnetic fields that are dynamically insignificant up to the moment of cloud destruction can inhibit thermal conduction and diffusion, those magnetic fields may become dynamically important as a result of turbulent amplification during the mixing phase. A fully magnetohydrodynamic description of the interaction of a strong shock with a system of clouds will need to be carried forward in future works.

This work was supported in part by the NSF grant AST 97-02484 and the Laboratory for Laser Energetics under DOE sponsorship. The most recent results and animations of the numerical experiments, described above and not mentioned in the current paper, can be found at http://www.pas.rochester.edu/~wma.

REFERENCES

Anderson, M. C., Jones, T. W., Rudnick, L., Tregillis, I. L., & Kang, H. 1994, ApJ, 421, L31
Arthur, S. J., Henney, W. J., & Dyson, J. E. 1996, A&A, 313, 897
Bedogni, R., & Di Fazio, A. 1998, Nuovo Cimento, 113, 1373
Berger, M. J., & Colella, P. 1989, J. Comput. Phys., 82, 64
Berger, M. J., & Jameson, A. 1985, AIAA J., 23, 561
Berger, M. J., & LeVeque, R. J. 1998, SIAM J. Numer. Anal., 35, 2298
Berger, M. J., & Oliger, J. 1984, J. Comput. Phys., 53, 484
Burkert, A., & O'Dell, C. R. 1998, ApJ, 503, 792
Dyson, J. E., & Hartquist, T. W. 1992, Astrophys. Lett., 28, 301
———. 1994, in 34th Herstmonceux Conf., Circumstellar Media in the Late Stages of Stellar Evolution, ed. R. Clegg, P. Meikle, & I. Stevens (Cambridge: Cambridge Univ. Press)
Gregori, G., Miniati, F., Ryu, D., & Jones, T. W. 1999, ApJ, 527, L113
———. 2000, ApJ, 543, 775
Hartquist, T. W., & Dyson, J. E. 1988, Ap&SS, 144, 615
Hartquist, T. W., Dyson, J. E., Pettini, M., & Smith, L. J. 1986, MNRAS, 221, 715
Jones, T. W., Ryu, D., & Tregillis, I. L. 1996, ApJ, 473, 365
Jun, B.-I., & Jones, T. W. 1999, ApJ, 511, 774
Jun, B.-I., Jones, T. W., & Norman, M. L. 1996, ApJ, 468, L59
Klein, R. I., McKee, C. F., & Colella, P. 1994, ApJ, 420, 213 (KMC94)
Kuncic, Z., Blackman, E. G., & Rees, M. J. 1996, MNRAS, 283, 1322
Landau, L. D., & Lifshitz, E. M. 1959, Fluid Mechanics (Reading: Addison-Wesley)
LeVeque, R. J. 1997, J. Comput. Phys., 131, 327
Lim, A. J., & Raga, A. C. 1999, MNRAS, 303, 546
Mac Low, M.-M., McKee, C., Klein, R., Stone, J. M., & Norman, M. L. 1994, ApJ, 433, 757
Miller, D. G., & Bailey, A. B. 1979, J. Fluid Mech., 93, 449
Miniati, F., Jones, T. W., & Ryu, D. 1999, ApJ, 517, 242
O'Dell, C. R., Weiner, L. D., & Chu, Y.-H. 1990, ApJ, 362, 226
Phillips, J. P., & Cuesta, L. 1999, AJ, 118, 2929
Poludnenko, A. Y., Frank, A., & Blackman, E. G. 2002, in ASP Conf. Ser. 255, Mass Outflow in Active Galactic Nuclei: New Perspectives, ed. D. M. Crenshaw, S. B. Kraemer, & I. M. George (San Francisco: ASP), 285
Redman, M. P., Williams, R. J. R., & Dyson, J. E. 1998, MNRAS, 298, 33